Design Analysis of a Novel Belt-Driven Manipulator for Fast Movements

Christoph Stoeffler[a,*], Janne Janzen[a], Adriano del Río[a], Heiner Peters[a]

***Abstract*— In this work, we propose a new four-degree-of-freedom (4-DOF) manipulator design involving belt transmissions and direct drives at the proximal end of the manipulator. This results into a backlash free, low-inertia arm enabling fast movements. Additionally, the belt routing inside the arm distributes actuator torques beneficially to the joints and allows the use of identical motors under dissimilar joint torque requirements. While the kinematics of the arm and the separation of actuation and joint space are discussed in detail, we also show beneficial properties for dynamic movements of the manipulator. To obtain optimal motion trajectories, an *iterative Linear-Quadratic Regulator* (iLQR) was implemented and is compared against a traditional trajectory creation in joint- and actuation space. Furthermore, a stiffness model of the belts in joint- and actuation-space is given to assess a modal analysis in the early design phase.**

I. INTRODUCTION

The kinematic performance of a robotic arm is mainly influenced by its geometry and overall topology. This performance issue is often addressed by gaining insight to the serial arrangements of links and joints. With a demand on faster moving robots and higher requirements on safety, e.g. human-robot interaction, the inertial properties obtain a very important role alongside. Whereas some weight improvements can be gained by structural optimization of manipulators, a significant improvement has been achieved by employing robots as parallel linkages in the past, allowing actuators to be placed more advantageously e.g. at the base of the robot [1]. This led to impressive improvements in terms of stiffness and speed with the *DELTA robot* being maybe the most prominent example [2]. Parallel robot topologies underly more kinematic constraints and by this transfer actuator movements non-linearly into task-space, what often reduces their dexterity and work space size considerably. In that sense, tendon-driven[1], serial robots can be seen as a combination of serial and parallel machines, possessing an outer serial structure with a kinematically coupled actuation underneath. While a reduction or amplification of actuator-to-joint movements is generally achieved, its magnitude remains configuration independent and therefore acts as a gear train. Tendon-driven manipulators however share with parallel robots the property of distinct joint- and actuator-space, as the motors are not collocated in the joints (see Fig. 1). This division must be addressed during analysis, design and control and can bring considerable advantages for actuation, like e.g. presented in [3].

[a]German Research Center for Artificial Intelligence, Robert-Hooke-Str. 1, 28359 Bremen, Germany firstname.lastname@dfki.de
*Corresponding author

[1]The term tendon encompasses belts, cables and similar transmissions, like suggested in [17]

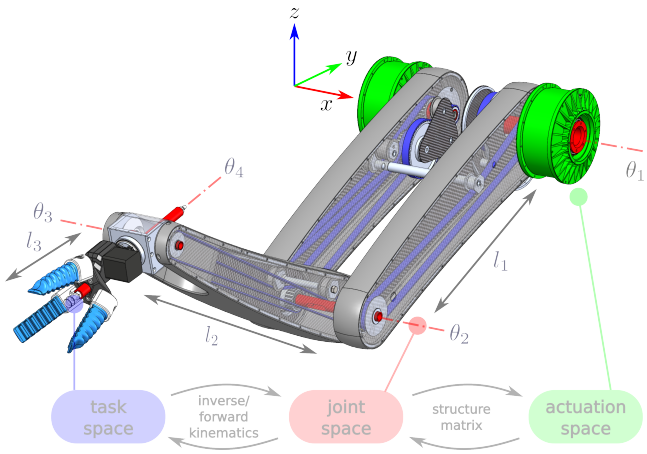

Fig. 1: Serial manipulator driven by belts that are inside the support structure of the arm. The belt routing results into a design with preferable mass distribution. Belt transmission allows four identical motors to be used. Courtesy gripper: Othmerding Maschinenbau GmbH & Co. KG

In this work, we introduce a novel robotic arm that is developed for fruit harvesting tasks which necessitates repetitive fast picking movements and high agility. In the current design state, the overall weight amounts to 5.3 kg, of which only 2.6 kg is accelerated mass for an additional payload capacity of 1 kg. This lightweight design is achieved by hollow link structures composed of a sintered plastic frame covered by carbon-fibre reinforced plastic sheets. These hollow structures also accommodate the belt transmissions. The arm has four active joints and is connected to a platform through another linear actuator in the harvesting scenario, making it a 5-DOF system. Via belt routing, all arm joints are driven from the base - see Fig. 2a. The manipulator's wrist is designed from a bevel differential gear and also obtains motion input from forward-running belts, allowing for combined pitch and roll movement. This design allows for the use of four identical motors instead of specifically sized drives per joint. By detailing the arms internal kinematics, we will show that not only the placement of actuators in the base is advantageous, but also a preferable torque distribution is induced. In order to have a mechanically transparent system, direct drives are used for actuation, where comparatively low reduction ratios can be realized in the belt transmissions directly. Envisaging dynamic control of the arm, optimal trajectories are created with an *iterative Linear-Quadratic Regulator* (iLQR) and a joint space stiffness model is also presented, revealing expected frequency modes for control.

II. STATE-OF-THE-ART

Belts have long been used to transmit rotational power and appeared in the factories of the first industrial revolution before they were gradually replaced by electric machines. Robots, on the other hand, may underly the opposite evolution. Whereas traditional serial manipulators are mostly equipped with geared electric drives in their joints, some developments have also been made in the direction of tendon-driven systems. One of the early works can be accounted to Salisbury and Jacobsen and their colleagues [4], [5], [6], adressing the issue of lightweight and stiff structures. Torque and motion transmission via cables has been shown effective for legged robots [7]. Similarly, the systems *LIMS1* and *LIMS2* were designed with the paradigm of low inertia and high stiffness, where the latter is mainly achieved by specific block and tackle mechanisms in the joints [8], [9]. In contrast to other tendon-driven systems, a kinematic coupling between actuation and joint-space is partly avoided by an elaborated mechanism in the elbow joints. More joint flexibility was introduced on purpose in *BioRob* [10] involving stiffness and damping models to account for dynamic controls of the arm. The kinematic coupling in this system is relatively simple, only affecting two subsequent joints. A higher coupling was used in [11] and also [12] what developed into a 10-m long manipulator with a payload capacity of 10 kg [13]. Amongst the load distribution in the tendons, this was achieved by adding a *weight compensation tendon* making it a redundantly actuated systems. These works are rooted in [14] which has similarities to the aforementioned designs ([4], [5]). Around this time, Tsai and Lee showed that kinematic analysis of tendon-driven mechanisms are analogical to that of epicyclic gear trains for which graph-based methods have been an effective tool [15]. Moreover, it has been shown that spatial systems can be represented by planar schematics, a fact we also used for the investigation of our arm. Due to the gear-like property of tendon-driven arms, the constant-linear map between joint- and actuation-space has been labeled as *structure matrix*. In our work, we also stick to this terminology. The formalization of kinematic analysis fueled developments in the direction of mechanism synthesis [16], [17], [18] and has a close relationship to research in general gear trains - see e.g [19].

In the last years much research has been conducted on soft robots and tendons are amongst others one favoured means of actuation for them. However, we limit this discussion to robots with a distinct joint space.

III. KINEMATICS

The arm possesses a simple outer topology composed of three successive revolute joints with parallel joint axes and an additional roll joint near the end-effector. Whereas all joints are belt-driven, the last two joints of this serial arrangement are executed as a bevel differential gear, making the last joint axis orthogonal to the others (see Fig. 2a). The three link lengths can be seen in Fig. 1, showing the axes and the associated joint angles $\boldsymbol{\theta} \in \mathbb{R}^4$

For brevity, we omit a presentation of the forward and inverse kinematics of the manipulator. The first can be computed by the *product of exponentials* (see e.g. [20, p. 137]) and the latter is computed by planar kinematics (see e.g. [21, p. 109]) in addition to one spatial rotation (last DOF of chain). Rather, the kinematic relation between motors and joints is established hereafter.

A. Actuation and Joint Space Maps - The Structure Matrix

The transfer between joint angles $\boldsymbol{\theta}$ and the motor angles $\boldsymbol{\mu}$ is expressed by the matrix $\boldsymbol{S}$ with

$$\boldsymbol{\mu} = \boldsymbol{S}\boldsymbol{\theta}. \tag{1}$$

The transpose of $\boldsymbol{S}$ is called structure matrix, of which we will give a detailed derivation based on the graph describing the system. For this purpose, the depicted belt routing of Fig. 2a is brought into a schematic overview that incorporates all belts, gear wheels and rigid connections in the system. Such a scheme can be seen in Fig. 2b, indicating the four actuated gear wheels in green and arm joints as red. Dashed lines show belt connections and solid square boxes a rigid attachment of a gear onto a link. The schematics of Fig. 2b

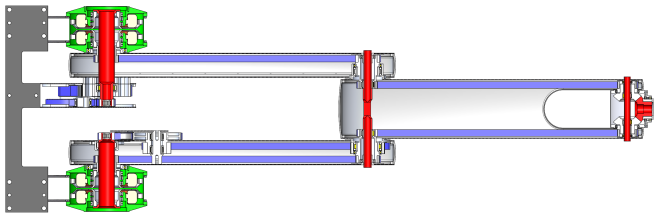

(a) Cross-section view of the manipulator with four identical motors (green) on the left. Belts are indicated blue and their routing is carried out by hollow shafts in the joints (red). The pitch and roll movement of the wrist (right) is gained from a bevel gear, driven by two belts.

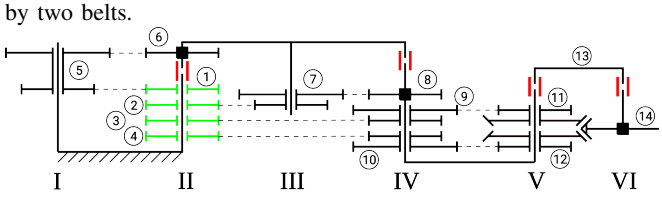

(b) Planar schematics derived from Fig. 2a with driven gear wheels in green and manipulator joints in red. The bevel gear arrangement between axis V and VI (i.e. joint three and four) is shown by the tapered wheel connections of wheel 11, 12 and 14

Fig. 2: Topological depiction of the arm that is used for the subsequent kinematic analysis

serves the graph representation of Fig. 3 by depicting gear wheel bearings and belts of the schematics by solid and dashed edges respectively. Links and wheels (bodies) are represented by numbered vertices - with ground being 0. Note that axis labels are also transferred and active wheels and joints are colored alike. The bevel gear connection of wheels 11 and 12 onto 14 is depicted as double dashed line in the graph. From here, we can make use of the *fundamental circuits* as detailed e.g. in [22] and allow to build the set of equations stemming from the *spanning tree* of the system. A

fundamental circuit $(a,b)(c)$, where vertices (bodies) a and b are connected by a dashed edge (belt) and both supported by the vertex (body) c results into the kinematic equation

$$\gamma_a^c = N_b^a \gamma_b^c. \tag{2}$$

It describes relative angles γ_a^c from body a to body c, such that $\gamma_c^a = -\gamma_a^c$ using the gear ratio N_b^a between body b and a, such that $N_a^b = 1/N_b^a$, by the relative angle γ_b^c. The gear ratio is a result of the effective wheel radi or teeth number: $N_b^a = r_a/r_b = n_a/n_b$. Moreover, a *coaxial* relation (a,b,c) - when bodies a, b and c share the same axis of rotation - is given by

$$\gamma_a^b = \gamma_a^c - \gamma_b^c. \tag{3}$$

From the graph of Fig. 3 the fundamental circuits can be directly obtained, exploiting the possibility to leap over vertices with identical edge connection. As an example the fundamental circuit $(2,7)(6)$ skips vertex 0 via edges II. In

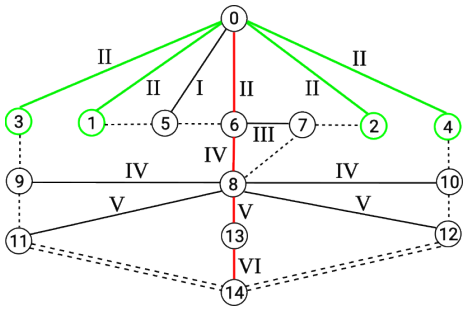

Fig. 3: Graph that represents the kinematic topology of the arm, where axes of input angles are depicted green and manipulator joints red. Due to closed-loop coupling in the edges 8, 11, 12, 13 and 14, the graph looses its spanning tree structure at that point.

order to solve the angle relationships for the entire graph, loop-closure equations have to be additionally formulated, as the vertices 13 and 14 do not belong to the spanning tree. Regarding bevel gear kinematics, they present simple linear equations and are directly listed in Tab. I.

TABLE I: Kinematically relevant relations

fundamental circuits	**coaxial relations**	**loop-closure equ.**
$(1,5)(0)$		
$(2,7)(6)$	$(0,2,6)$	
$(3,9)(6)$	$(0,3,6)$	
$(4,10)(6)$	$(0,4,6)$	$\theta_{13}^8 = 1/2(\theta_{11}^8 + \theta_{12}^8)$
$(5,6)(0)$	$(8,9,6)$	$\theta_{14}^{13} = 1/2(\theta_{11}^8 - \theta_{12}^8)$
$(7,8)(6)$	$(8,9,10)$	
$(9,11)(8)$	$(8,10,6)$	
$(10,12)(8)$		

The matrix $\boldsymbol{S}$ is obtained from the set of circuit- and coaxial-equations given in Tab. I using (2) and (3), augmented by the loop-closure equations of Tab. I. Isolating $\boldsymbol{\theta} = [\gamma_0^6 \quad \gamma_6^8 \quad \gamma_8^{13} \quad \gamma_{13}^{14}]^T$ from $\boldsymbol{\mu} = [\gamma_0^1 \quad \gamma_0^2 \quad \gamma_0^3 \quad \gamma_0^4]^T$ in this set of linear equations reveals

$$\boldsymbol{S}^T = \begin{bmatrix} 1/g_1 & 1 & 1 & 1 \\ 0 & 1/g_2 & 1/g_3 & 1/g_4 \\ 0 & 0 & 1/g_5 & 1/g_6 \\ 0 & 0 & 1/g_5 & -1/g_6 \end{bmatrix} \tag{4}$$

where the vector of positive gear ratios writes

$$\boldsymbol{g} = \begin{bmatrix} g_1 \\ g_2 \\ g_3 \\ g_4 \\ g_5 \\ g_6 \end{bmatrix} = \begin{bmatrix} N_1^5 N_5^6 \\ N_2^7 N_7^8 \\ N_3^9 \\ N_4^{10} \\ N_3^9 N_9^{11} \\ N_4^{10} N_{10}^{12} \end{bmatrix} \tag{5}$$

and incorporates all transmission ratios of the manipulator. Due to the symmetry of the transmissions in our design, we further have $g_3 = g_4$ and $g_5 = g_6$, what leaves (4) with a simpler structure. This is the case when the forward running belts on both sides of the $y-z$-plane have the same reduction ratios.

Looking at the time derivative of (1) one gets

$$\dot{\boldsymbol{\mu}} = \boldsymbol{S}\dot{\boldsymbol{\theta}} + \underbrace{\dot{\boldsymbol{S}}\boldsymbol{\theta}}_{=0}.$$

The virtual power from torque $\boldsymbol{\tau}$ and speed $\dot{\boldsymbol{\theta}}$ in joint space must be equal to the power in the motors, giving

$$\boldsymbol{\tau}^T \boldsymbol{S}^{-1} \dot{\boldsymbol{\mu}} = \boldsymbol{\zeta}^T \dot{\boldsymbol{\mu}}$$

with $\boldsymbol{\zeta}$ and $\dot{\boldsymbol{\mu}}$ being motor torque and speed respectively and what can only hold true (no zeros in $\dot{\boldsymbol{\mu}}$ assumed) if

$$\boldsymbol{\tau} = \boldsymbol{S}^T \boldsymbol{\zeta}. \tag{6}$$

The *pseudotriangular* structure of $\boldsymbol{S}$ can leverage advantageous torque distributions from actuation- to joint-space when the motor torques act in the same rotation direction. However, there can occur serious energy losses due to a possible antagonism of the drives like described in [23] and has to be taken into account for the creation of optimal trajectories. This will be further investigated in Sec. VI-B

IV. STIFFNESS MODELS

In the present design, distances of almost half a meter are bridged with slender belts and by this, they introduce an inherent compliance to the manipulator. The compliant behaviour of the system may become critical for dynamics based control. A stiffness description in joint space coordinates is thus indispensable for this design. In general, stiffness in any space is defined as the first-order-term of the *Taylor expansion* of force $\boldsymbol{f}$ with respect to displacement $\boldsymbol{s}$, such that

$$\boldsymbol{K} = \frac{d\boldsymbol{f}}{d\boldsymbol{s}}. \tag{7}$$

Differentiating (6) and making use of (7) in actuation- and joint-space yields

$$
\begin{aligned}
d\boldsymbol{\tau} &= \underbrace{(d\boldsymbol{S}^T)\boldsymbol{\zeta}}_{=0} + \boldsymbol{S}^T(d\boldsymbol{\zeta}) \\
\boldsymbol{K}_\theta d\boldsymbol{\theta} &= \boldsymbol{S}^T \boldsymbol{K}_\mu d\boldsymbol{\mu} \\
\boldsymbol{K}_\theta &= \boldsymbol{S}^T \boldsymbol{K}_\mu \boldsymbol{S} \qquad (8)
\end{aligned}
$$

The matrix $\boldsymbol{K}_\mu$ is diagonal, since any force changes at the motors are only function of the related motor displacements itself and depend on the serially connected belts. Its computation is part of the subsequent section. In contrast, $\boldsymbol{K}_\theta$ is a symmetric matrix, due to the congruence transformation that the structure matrix puts onto $\boldsymbol{K}_\mu$ in (8).

A. Stiffness in Actuation Space

To obtain stiffness values in actuation space, we make use of a lumped-parameter model that assumes a rotational stiffness over the motor coordinates, which stems from the serially connected belts over different gearwheel radi, as depicted in Fig. 4. For the derivation of our model, the following assumptions are made:

- Small deflections of the involved parts, such that (7) holds
- Structural stiffness of the manipulator links and gearwheels is not included and thus considered rigid.
- Tensioned belt lengths (blue segments of Fig. 4) are assumed to be constant for one stage and independent of the direction of rotation, neglecting e.g. one sided tensioner pulleys.

In Fig. 4 a gear stage with $n = 3$ subsequent belts is shown, where we will give a stiffness expression for general n belts. By convention, the first belt is on the motor side of the system and the last belt n on the actuated joint side, where this joint is considered fixed for our discussion. An

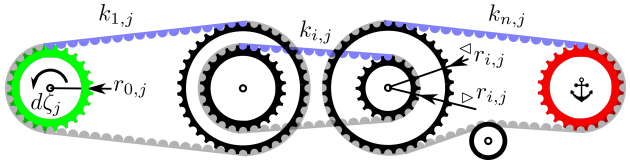

Fig. 4: Schematics of a three-stage belt transmission, with driven wheel (green), actuated joint (red) and belts under tension (blue). The serially connected belts give rise to the lumped-element stiffness of Equ. (14) around motor angle μ_j

expression for the equivalent longitudinal stiffness of the serially connected belts $\bar{k}_j$ at every motor is derived. It is the apparent stiffness seen at the first motor driven belt by considering the serial connection of all subsequent belts in the chain. Taking the radius of the motor driven wheel $r_{0,j}$, the (rotational) actuation space stiffness is obtained from a virtual work relation by $k_j = r_{0,j}^2 \bar{k}_j$. The equivalent longitudinal belt stiffness at motor j can be computed by considering its force-displacement relationship, such that

$$
\frac{1}{\bar{k}_j} = \frac{ds_{1,j}}{dF_{1,j}} \qquad (9)
$$

where $dF_{1,j}$ is the differential force acting on the first belt (left in Fig. 4) and $ds_{1,j}$ the total displacement under that force. We further have

$$
ds_{1,j} = \sum_{i=1}^{n} ds'_{i,j} \qquad (10)
$$

$$
ds'_{i,j} = ds_{i,j} \prod_{l=1}^{i-1} \frac{{}^{\triangleleft}r_{l,j}}{{}_{\triangleright}r_{l,j}} \qquad (11)
$$

where it is considered that the total displacement in the first stage results from all subsequent belt displacements $ds'_{i,j}$ that undergo changes due to serially combined gear stages - accounted by (11). The symbols ${}_{\triangleright}r_{l,j}$ and ${}^{\triangleleft}r_{l,j}$ denote the input and output radi of every gear stage like shown in Fig. 4. Note that the running index i for the gear transmissions in (11) changes to l due to the nested sequence inside the series and we define the product to return one if: $i-1 < l$. Lastly, stiffness and force change in every belt stage are given by

$$
k_{i,j} = \frac{dF_{i,j}}{ds_{i,j}} \qquad (12)
$$

$$
dF_{i,j} = dF_{1,j} \prod_{l=1}^{i-1} \frac{{}^{\triangleleft}r_{l,j}}{{}_{\triangleright}r_{l,j}} \qquad (13)
$$

Combining (9) - (13) finally yields

$$
\frac{1}{\bar{k}_j} = \sum_{i=1}^{n} \left[\frac{1}{k_{i,j}} \prod_{l=1}^{i-1} \left(\frac{{}^{\triangleleft}r_{l,j}}{{}_{\triangleright}r_{l,j}} \right)^2 \right]. \qquad (14)
$$

In order to get an expression for $\boldsymbol{K}_\mu$, the following steps can be pursued

1) Determine all active belt connections for every motor j from the graph (Fig. 3) by passing from motor joint (green vertices) over all directly connected dashed edges until no further single dashed edge can be passed.
2) Geometrically determine the active belt lengths $L_{i,j}$ (blue segments in Fig. 4) and compute their longitudinal stiffness values $k_{i,j} = \kappa_{i,j}/L_{i,j}$. Here $\kappa_{i,j}$ is the length specific stiffness of the belt that can usually be obtained from the manufacturer.
3) Compute the equivalent translational stiffness $\bar{k}_j$ from (14) and bring it into a rotational stiffness for every joint by $k_j = r_{0,j}^2 \bar{k}_j$. From there the diagonal actuation-space stiffness matrix $\boldsymbol{K}_\mu = \mathrm{diag}(k_1, \ldots, k_n)$ can be constructed.

V. PHYSICAL PARAMETERS

We quickly give a rather incomplete overview about our design specifications to leave the reader with an idea of the overall layout, before assessing its performance. Specifically designed motors with hollow shaft and a maximum torque of $\zeta_j^{max} = 6\,\mathrm{Nm}$ are used for actuation. The link lengths are $l_1 = 0.4\,\mathrm{m}$, $l_2 = 0.4$ and $l_3 = 0.1$ with masses of

1.63 kg, 0.78 kg and 0.18 kg respectively in the first design stage. Without listing explicitly all gear ratios of (5), we instead give the expression for the structure matrix directly, that writes

$$\boldsymbol{S}_{build}^{T} = \begin{bmatrix} 6 & 1 & 1 & 1 \\ 0 & 4.5 & 1 & 1 \\ 0 & 0 & 1 & 1 \\ 0 & 0 & 1 & -1 \end{bmatrix}$$

what results into the joint-space stiffness

$$\boldsymbol{K}_{\theta}^{build} = \begin{bmatrix} 17623 & 1402 & 213 & 0 \\ 1402 & 5566 & 213 & 0 \\ 213 & 213 & 213 & 0 \\ 0 & 0 & 0 & 213 \end{bmatrix} \text{Nm/rad}$$

showing very high stiffness, notably in the first two joints. Here, belts with relative stiffness κ of 196.75 N/mm and 335.5 N/mm are installed. Due to the internal belt coupling, joint-space stiffness is considerably higher compared e.g. to [8], while the arm inertia of 0.65 kgm^2 measured towards its base is comparable to that design [24]. The high stiffness is also rendered in Sec. VI. It was found that for other arm topologies and different gear ratios, joint-space stiffness can forfeit considerably, owing to the quadratic dependency on gear ratio and the kinematic back-coupling.

VI. PERFORMANCE ANALYSIS

For the dynamic simulation of the manipulator, we made use of the `RigidBodyDynamics.jl` package, being part of [25] and able to compute gradients of the equation of motion by *automatic differentiation*. Also, it provides an URDF parser, which we used for a simple incorporation of the dynamic parameters on joint-space level. These functionalities allow to quickly implement and test e.g. *indirect methods* in optimal control. [2] Since introduced belt compliance on joint level might require further efforts in stabilizing the arm, its frequency response behaviour is investigated first.

A. Frequency Modes of the Manipulator

Equation (8) allows to compute the joint-space stiffness of the arm, in which also its mass matrix is naturally expressed when using minimal coordinates. The *eigenmodes* of a flexible system can be computed by solving the *generalized eigenvalue problem*

$$(\boldsymbol{K}_{\theta} - \omega^2 \boldsymbol{M})\boldsymbol{v} = 0$$

where $\boldsymbol{M}$ is the configuration dependent mass matrix, ω the eigenfrequency in radians per second and $\boldsymbol{v}$ the vector that describes the eigenmode of the system [26]. The manipulators joint-space eigenfrequencies are depicted in Fig. 5 for several random poses and a payload mass of 1 kg. It shows how much each joint "contributes" to every sampled mode, indicating that joint 4 is decoupled in mass and stiffness matrix from the other DOFs. It thus exhibits a single eigenfrequency of 73.4 Hz (see upper plot value) that

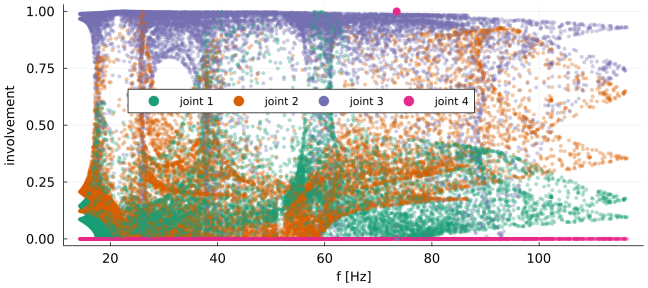

Fig. 5: Random sampling of eigenfrequencies for $\theta_i \in (-\pi, \pi)$ with 5000 samples. "Involvement" is the magnitude of the related eigenvector value relative to its unit length at a sampled pose to show which joints are mostly affected.

directly depends on the end-effector and payload mass distribution though. Joint 3 shows overall the highest oscillation involvement, suggesting that the related belt stiffness could be adapted for the present design. Eigenmodes below 15 Hz do not have to be expected, but some configurations with frequencies below 20 Hz exist. Whereas Fig. 5 asserts that a wide range of frequencies is present in the current design, it can be assumed that high frequency content will be absorbed by damping of the system.

B. Control Trajectories in Joint- and Actuation-Space

Since the aim of the manipulator is to perform fast picking tasks, we employed an optimal control approach to create trajectories that can assess its dynamic capabilities. To this end, we pursued an iLQR-implementation detailed in [27] solving the discretized trajectory optimization problem split into $N-1$ intervalls:

$$\begin{aligned} \min_{\boldsymbol{x}_{1:N}, \boldsymbol{u}_{0:N-1}} \quad & \ell_f(\boldsymbol{x}_N) + \sum_{k=0}^{N-1} \ell(\boldsymbol{x}_k, \boldsymbol{u}_k) \\ \text{subject to} \quad & \boldsymbol{x}_{k+1} = f(\boldsymbol{x}_k, \boldsymbol{u}_k) \end{aligned} \tag{15}$$

with ℓ_f and ℓ as the user defined, quadratic cost functions for final and intermediate state respectively. States $\boldsymbol{x}_k$ and controls $\boldsymbol{u}_k$ at time instant k are input to the discrete system dynamics $f(\boldsymbol{x}_k, \boldsymbol{u}_k)$, which were obtained by applying an explicit fourth-order Runge-Kutta interpolation on the continuous dynamics. As the rotational inertia of the end-effector possesses very low values, the ill-conditioning of the arms mass-matrix showed challenges in the computation of the algorithm. Therefore, this rotational inertia was increased by one order of magnitude. Since motion trajectories without rotation in the last joint are considered in the following, this poses no problem. Relative motion of parts, like in gears and belts is neglected in the dynamics simulation, assuming only a four-rigid-body model. Furthermore, a *regularization* strategy has been applied to the Hessian of the interpolated

[2]The code to the paper can be found under: `github.com/dfki-ric-underactuated-lab/BeltManipulator`.

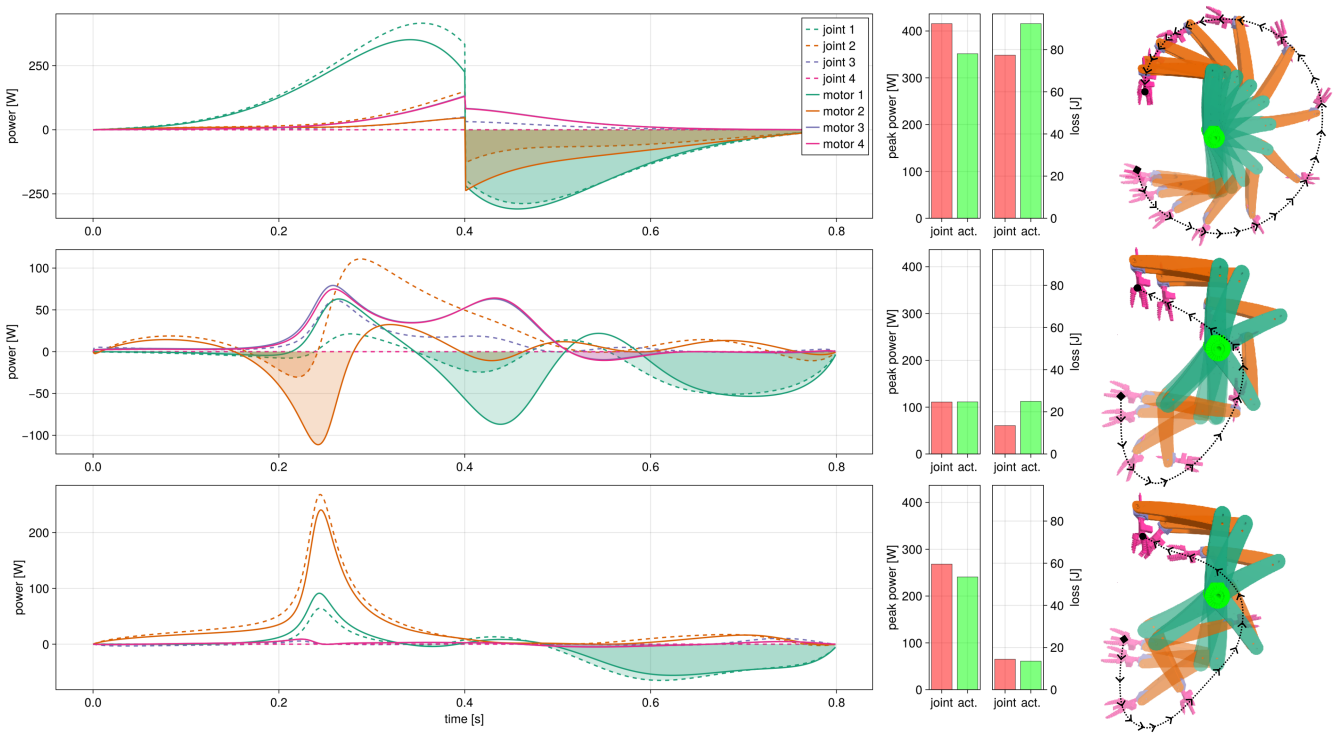

Fig. 6: Motor power distributions in joint- and actuation-space for the trajectories under consideration that are depicted as snap-shots on the right. Shaded areas indicate negative power and thus energy losses that are accumulatively given as bar plots together with the maximum occurring motor powers.

action-value function in the *backward pass* of the iLQR to improve stability of the computations. A detailed explanation is presented in [27]. We showcase the importance of optimal trajectories for a repetitive pick and place task in a harvesting scenario. A motion from $\boldsymbol{\theta}_0 = [0 \quad 0.6\pi \quad 0 \quad 0]^T$ to $\boldsymbol{\theta}_f = -[\pi \quad \pi/2 \quad \pi/2 \quad 0]^T$ is executed in $t_f = 0.8\,\mathrm{s}$ under gravity with $\dot{\boldsymbol{\theta}}_0 = \dot{\boldsymbol{\theta}}_f = \mathbf{0}$ and a payload mass of 1 kg. This task is addressed with three different actuation cases:

1) Traditional approach, where joint-space positions and velocities are obtained from the integral of the required accelerations to overcome $\boldsymbol{\theta}_f - \boldsymbol{\theta}_0$ in t_f. This assumes constant accelerations $\boldsymbol{a}_c$ at time $t \in [0, t_f/2)$ and $-\boldsymbol{a}_c$ at $t \in (t_f/2, tf]$, such that $\boldsymbol{a}_c = 4(\boldsymbol{\theta}_f - \boldsymbol{\theta}_0)/t_f^2$. Joint torques are then obtained from the *recursive Newton-Euler* algorithm in `RigidBodyDynamics.jl`.
2) Joint torques are computed by the outlined iLQR method, assuming actuation in joint-space - like most optimal control frameworks.
3) Actuator torques are considered as optimization input to (15) and are therefore mapped by (6) inside the system dynamics. Inertia, gravity and coriolis terms are still considered in joint-space.

In order to compare the three different approaches, motor power - the product of torque and velocity - is considered, since this quantity is invariant under transformations to joint- or actuation-space. This is also convenient from the point that it eliminates the consideration of belt-gear ratios. However, in a more thorough examination, friction would also need to be taken into account. The motor power results in both spaces and spatial motions from actuation case 1) to 3) can be seen in Fig. 6 from top to bottom. Note that no movement is intended for joint 4 and due to the bevel-gear coupling in the wrist, motor 3 and 4 show (with slight deviation in case 2)) the same trajectories in actuation-space. The shaded areas in the power plots show the integral of negative power and thus the energy loss occurring during task execution. Actuation case 1) entails a task-space trajectory, where the arm traverses a stretched position, what is generally an unfavorable dynamic behavior and results in high joint torques and therefore the highest power requirements. When this trajectory is mapped into actuation-space, a slight power reduction under increased energy loss can be observed. Applying the provided iLQR to this planning problem in joint-space (center plot of Fig. 6), shows considerable improvements compared to case 1), as peak-power and energy losses are noticeably decreased. Providing the iLQR with actuation kinematics, results in further improvements as shown in case 3) where the energy losses are least at the cost of higher peak power requirements. However, the power requirements are still within the specifications of the motors. Specifically for fast pick and place tasks with a high repetition rate, energy-efficient behavior is favorable. In order to converge to solutions with identical goal state for case 2) and 3), different weights in the cost function had to be used and can be subject to further changes, if varying power trajectories are desired.

VII. CONCLUSION AND FUTURE WORK

We introduced a novel, belt-driven, serial manipulator with the detailed description of its belt kinematics and a general form to obtain the underlying mapping between joint- and actuation space. This was extended by a stiffness model accounting for the compliance brought in by the belts. We were able to show that this results into a sufficient stiff design, when large deflections are undesirable and exemplified the high dynamic capability of the manipulator by motion trajectories for a typical use case. It showed to be beneficial when the belt routing is incorporated in the manipulator dynamics during trajectory optimization.

As this work presents a first prototype, further improvements are envisaged for the design and the behaviour generation in general. For example, the consideration of inequality constraints in the trajectory optimization would be beneficial in application scenarios, where collisions must be avoided. While other belt routings, altered gear ratios and changed geometries are thinkable, this topology - even though very simple in its outer structure - leaves much room for synthesis and design optimality. We believe that new capabilities for manipulators can arise under this concept and plan to take an optimized, more generic concept into account.

ACKNOWLEDGMENT

The authors would like to thank all members of the project team for their help and work. The activities described in this paper are part of the project RoLand with support from the Federal Ministry of Food and Agriculture (BMEL) by decision of the German Bundestag. The Federal Office for Agriculture and Food (BLE) provides coordinating support for artificial intelligence in agriculture as funding organisation, grant number 28DK103A20 / 28DK103B20 / 28DK103C20.

REFERENCES

[1] J. P. Merlet, Parallel Robots, Springer, 2010

[2] R. Clavel, DELTA, a fast robot with parallel geometry, Proc. of the 18th International Symposium on Industrial Robots, pp.91–100

[3] D. Mronga and S. Kumar and F. Kirchner, Whole-Body Control of Series-Parallel Hybrid Robots. IEEE International Conference on Robotics and Automation, 2022, pp.228–234

[4] J. K. Salisbury, Kinematic and Force Analysis of Articulated Hands, PhD thesis, Dep. of Mechanical Engineering, Stanford University, 1982

[5] S. C. Jacobsen and E. K. Iversen and D.F. Knutti and R. T. Johnson and K. B. Biggers, Design of the UTAH/M.I.T. Dextrous Hand, IEEE International Conference on Robotics and Automation, 1986, pp.1520–1532

[6] J.K. Salisbury and W.T. Townsend and B.S. Eberman and D.M. Dipietro, Preliminary design of a whole-arm manipulation system (WAMS), IEEE International Conference on Robotics and Automation, 1988, pp.254–260

[7] J. Hwangbo and V. Tsounis and H. Kolvenbach and M. Hutter, Cable-Driven Actuation for Highly Dynamic Robotic Systems, IEEE International Conference on Intelligent Robots and Systems, 2018, pp.8543–8550

[8] Y.-J. Kim, Anthropomorphic Low-Inertia High-Stiffness Manipulator for High-Speed Safe Interaction, IEEE Transactions on Robotics, vol. 33, 2017, pp.1358–1374

[9] H. Song and Y.-S. Kim and J. Yoon and S.-H. Yun and J. Seo and Y.-J. Kim, Development of Low-Inertia High-Stiffness Manipulator LIMS2 for High-Speed Manipulation of Foldable Objects, IEEE International Conference on Intelligent Robots and Systems, 2018, pp.4145–4151

[10] T. Lens and O.v. Stryk, Design and dynamics model of a lightweight series elastic tendon-driven robot arm, IEEE International Conference on Robotics and Automation, 2013, pp.4512–4518

[11] K. Yokoi and K. Komoriya and K. Tanie, Development of a coupled tendon drive manipulator with seven degrees-of-freedom, RoManSy 9, 1993, pp.339–346

[12] A. Horigome and H. Yamada and G. Endo and S. Hirose and E. F. Fukushima, Development of a Coupled Tendon-Driven 3D Multi-joint Manipulator, IEEE International Conference on Robotics and Automation, 2014, pp.5915–5920

[13] G. Endo and A. Horigome and Atsushi Takata, Super Dragon: A 10-m-Long-Coupled Tendon-Driven Articulated Manipulator, IEEE Robotics and Automation Letters, vol. 4, 2019, pp.934–941

[14] S. Ma and S. Hirose and H. Yoshinada, Design and Experiments for a Coupled Tendon-Driven Manipulator, IEEE International Conference on Robotics and Automation, 1992, pp.30–36

[15] L.-W. Tsai and J.-J. Lee, Kinematic Analysis of Tendon-Driven Robotic Mechanisms Using Graph Theory, Journal of Mechanisms, Transmissions, and Automation in Design, vol. 111, 1989, pp.59–65

[16] S.-L. Chang and L.-W. Tsai, Topological Synthesis of Articulated Gear Mechanisms, IEEE Trans. on Robotics and Automation, vol. 6, 1990, pp.97–103

[17] J.-J. Lee and L.-W. Tsai, The Structural Synthesis of Tendon-Driven Manipulators Having a Pseudotriangular Structure Matrix, The International Journal of Robotics Research, vol. 10, 1991, pp.255–262

[18] J.-B. Sheu and J.-J. Lee, Synthesis of Tendon-Driven Manipulators with High Fault Tolerance, IEEE Intern. Conf. on Systems, Man and Cybernetics, 2009, pp.4137–4142

[19] H.-L. Xue and G. Liu and X.-H. Yang, A review of graph theory application research in gears, Journal of Mechanical Engineering Science, vol. 230, 2016, pp.1697–1714

[20] K. M. Lynch and F. C. Park, Modern Robotics: Mechanics, Planning, and Control, Cambridge University Press, 2017

[21] J. J. Craig, Introduction to Robotics: Mechanics, and Control, Third Edition, Pearson Education, Inc., 2005

[22] O. Shai and K. Preiss, Graph theory representation of engineering systems and their embedded knowledge, Artificial Intelligence in Engineering, vol. 13, Elsevier, 1999, pp.273–285.

[23] A. Abate and J. W. Hurst and R. L. Hatton, Mechanical Antagonism in Legged Robots, Robotics: Science and Systems, vol. 12, 2016

[24] Y.-J. Kim, Design of Low Inertia Manipulator with High Stiffness and Strength Using Tension Amplifying Mechanisms, IEEE International Conference on Intelligent Robots and Systems, 2015, pp.5850–5856

[25] T. Koolen and R. Deits, Julia for robotics: simulation and real-time control in a high-level programming language, IEEE International Conference on Robotics and Automation, 2019, pp.604–611

[26] M. Géradin and D. J. Rixen, Mechanical Vibrations: Theory and Application to Structural Dynamics, 3rd Edition, John Wiley & Sons, Ltd, 2015

[27] B. E. Jackson, AL-iLQR Tutorial, https://api.semanticscholar.org/CorpusID:209455095, 2019